The direct precipitation of rhabdophane ($REEPO_4 \cdot nH_2O$) nano-rods from acidic aqueous solutions at 5–100 °C

Teresa Roncal-Herrero, Juan Diego Rodríguez-Blanco, Eric H. Oelkers & Liane G. Benning

Journal of Nanoparticle Research
An Interdisciplinary Forum for
Nanoscale Science and Technology

ISSN 1388-0764
Volume 13
Number 9

J Nanopart Res (2011) 13:4049-4062
DOI 10.1007/s11051-011-0347-6

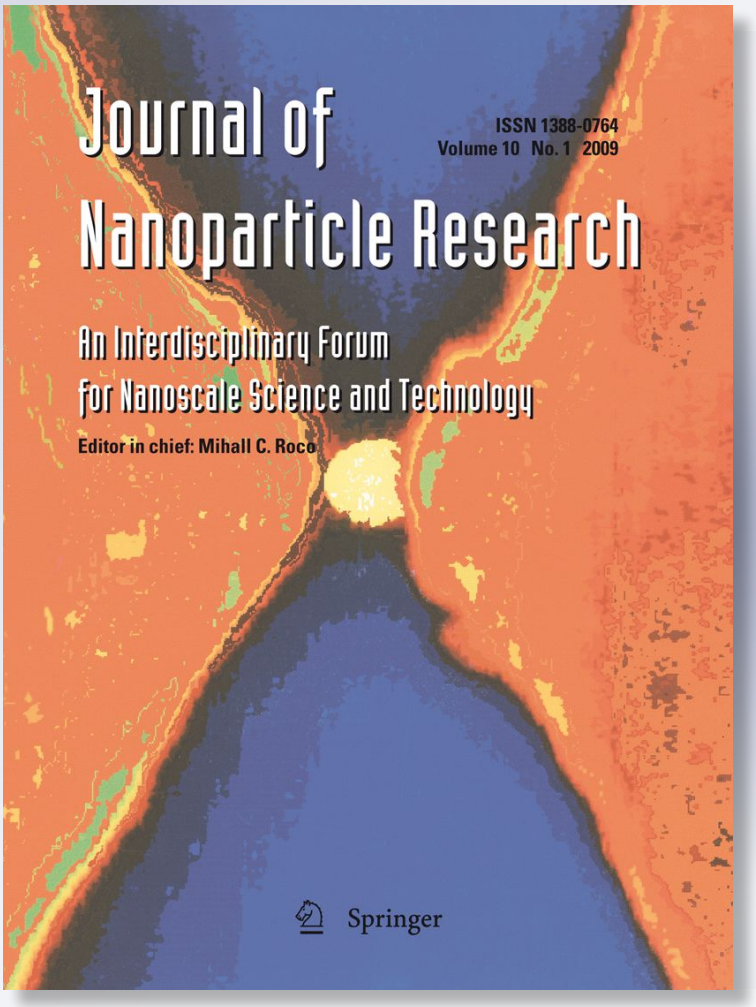

Springer

J Nanopart Res (2011) 13:4049–4062
DOI 10.1007/s11051-011-0347-6

RESEARCH PAPER

The direct precipitation of rhabdophane ($REEPO_4{\cdot}nH_2O$) nano-rods from acidic aqueous solutions at 5–100 °C

Teresa Roncal-Herrero · Juan Diego Rodríguez-Blanco · Eric H. Oelkers · Liane G. Benning

Received: 19 August 2010 / Accepted: 13 March 2011 / Published online: 2 April 2011

Abstract The precipitation of lanthanum and neodymium phosphate phases from supersaturated aqueous solutions at pH ~1.9 was studied at 5, 25, 50, and 100 °C in batch reactors for up to 168 h. Crystalline La and Nd–rhabdophane phases precipitated immediately upon mixing of the initial aqueous La or Nd and PO_4 solutions. Changes in aqueous PO_4 and Rare Earth Element (REE) concentrations during the experiments were determined by ICP-MS and UV–Vis spectrophotometry, while the resulting solids were characterized via powder XRD, SEM, TEM, and FTIR. All precipitated crystals exhibited a nano-rod morphology and their initial size depended on temperature and REE identity. At 5 °C and immediately after mixing the La and Nd–rhabdophane crystals averaged ~44 and 40 nm in length, respectively, while at 100 °C lengths were ~105 and 94 nm. After 168 h of reaction, the average length of the La and Nd rhabdophanes increased by 23 and 53% at 5 °C and 11 and 59% at 100 °C, respectively. The initial reactive solutions in all experiments had activity quotients for rhabdophane precipitation: $REE^{3+} + PO_4^{3-} + nH_2O = REEPO_4 \cdot nH_2O$ of $\sim 10^{-20.5}$. This activity quotient decreased with time, consistent with rhabdophane precipitation. The rapid equilibration of rhabdophane supersaturated solutions and the progressive rhabdophane crystal growth observed suggests that the REE concentrations of many natural waters may be buffered by rhabdophane precipitation. In addition, this data can be used to guide crystallization reactions in industrial processes where monodisperse and crystalline La or Nd rhabdophane materials are the target.

Keywords Nano-rods · Phosphate · Rare earth elements · Crystallization · Rhabdophane

T. Roncal-Herrero · J. D. Rodríguez-Blanco · L. G. Benning
School of Earth and Environment, University of Leeds, LS2 9JT Leeds, UK

T. Roncal-Herrero (✉) · E. H. Oelkers
Géosciences Environnement Toulouse, GET-Université de Toulouse-CNRS-IRD-OMP, 14 rue Edouard Belin, 31400 Toulouse, France
e-mail: eartr@leeds.ac.uk

Introduction

Rare Earth Element (REE) phosphate phases have been of increased industrial interest during the last decade due to their physical and chemical properties (e.g., resistance to corrosion and low solubility) and their potential use in making ceramics for nuclear waste storage host analogs (Chaïrat et al. 2007). Although in nature REE–rhabdophane phases may play a significant role in controlling the REE concentrations of waters and soils (Jonasson et al. 1985; Byrne and Kim 1993; Braun et al. 1998; Hongbing et al. 2004; Köhler et al. 2005), little is

known about their precipitation pathways and characteristics. The goal of this study is to provide an improved understanding of La and Nd–rhabdophane precipitation through a series of controlled laboratory experiments.

Phosphates of the rhabdophane group have a chemical formula $XPO_4{\cdot}nH_2O$ where X stands for REE, Y, Ca, Pb, Th, U, Fe; and n represents the number of water molecules in the structure which varies from 0.5 to 2. Rhabdophane has a hexagonal structure with large channels in the c direction (Mooney 1950), which are able to incorporate non-stoichiometric water (Kijkowska et al. 2003). REE-phosphates are commonly used in industry due to their luminescent properties, low solubility, and high stability. For example, they are components in optical amplification devices and plasma display panels (Rao and Devine 2000), in solid-state fuel cells (Norby and Christiansen 1995), laser materials (Nedelec et al. 2002), and in nuclear waste storage host analogs (Chaïrat et al. 2007; Oelkers and Montel 2008). A number of previous studies provided insight into the precipitation of REE-phosphates via a number of pathways including precipitation from aqueous solution (Min et al. 2000; Lucas et al. 2004; Zhang and Guan 2005; Bregiroux et al. 2006), sol–gel precipitation (Rajesh et al. 2007; Gao et al. 2010), and solid-state reactions through mechano-chemical methods (Onoda et al. 2003; Diaz-Guillén et al. 2007; Campayo et al. 2007).

In nature, REE-phosphates are released into the environment via the alteration of REE-bearing igneous minerals (Mitchell 1965; Oelkers et al. 2008), and from the dissolution of REE-rich apatites (Köhler et al. 2005; Taunton et al. 2000; Gaillardet et al. 2003). These processes lead to relatively low La and Nd concentrations in natural waters (i.e., rivers, oceans). For example, in river waters La and Nd concentrations range from 10 to 936 pmol/L and 7.94 to 1070 pmol/L, respectively (Gaillardet et al. 2003), while in sea water, the concentrations of La range between 16.5 and 82.3 pmol/L (De Baar et al. 1983) and of Nd from 46.3 to 359.8 pmol/L (Jeandel et al. 1995). Due to the limited mobility and similar chemical behavior of REE in aqueous environments, they have been used extensively as chemical tracers of natural fluid–rock processes (Fee et al. 1992; Jeandel et al. 1995; Johannesson et al. 2000; Hannigan and Sholkovitz 2001; Borrego et al. 2005; Tanaka and Kawabe 2006; Andersson et al. 2008; Mourier et al. 2008; Welch et al. 2009).

Although a number of studies evaluated the solubility of REE-phosphate at various temperatures by monitoring the fluid composition during rhabdophane dissolution (Liu and Byrne 1997; Firsching and Brune 1991; Cetiner et al. 2005), the reported solubilities vary by $\sim$2 orders of magnitude. Similarly, previous studies demonstrated that rhabdophane can be readily synthesized (Min et al. 2000; Lucas et al. 2004; Zhang and Guan 2005; Bregiroux et al. 2006; Rajesh et al. 2007; Gao et al. 2010; Onoda et al. 2003; Diaz-Guillén et al. 2007; Campayo et al. 2007), but a quantitative evaluation of the precipitated solids and the fluid compositional evolution during precipitation is lacking. This study aims to improve our understanding of REE-phosphate precipitation in natural and industrial processes through a systematic investigation of precipitation La and Nd rhabdophane from acidic aqueous solutions as a function of time and temperature.

Materials and methods

Rhabdophane was synthesized by mixing an aqueous solution of either 0.1 M $La(NO_3)_3{\cdot}9H_2O$ or $Nd(NO_3)_3{\cdot}9H_2O$ with an aqueous solution containing 0.1 M KH_2PO_4 and 0.09 M KOH. The concentrations were chosen to assure the supersaturation with respect to rhabdophane in the initial reactive solution. All solutions were prepared with 18 MΩ cm^{-1} Milli-Q grade water and brought to the experimental temperature before mixing. The experiments were performed in 200 mL borosilicate glass batch reactors at 5, 25, 50, and 100 °C. The two aqueous solutions were mixed in the glass reactors by simultaneous adding equal volumes of the initial solutions. The reactors were immediately sealed and placed in an oven or refrigerator at the desired temperature for up to 168 h. The pH of the initial $La(NO_3)_3{\cdot}9H_2O$, $Nd(NO_3)_3{\cdot}9H_2O$, and KH_2PO_4/KOH stock solutions were 1.2, 1.3, and 4.8, respectively, and the pH of all the initial mixed solutions were 1.9. pH was measured at 25 °C with an ORION pH-meter and a Toledo electrode calibrated with NBS standard buffer solutions. Experiments were performed at low pH because REE are more soluble at these conditions (Tosiani et al. 2004), and to avoid

precipitation of $La(OH)_3$ and $Nd(OH)_3$ that might occur due to their low solubility at pH $\sim$6 (Wood 1990; Smedley 1991), allowing accurate analysis of the fluid phase composition during the experiments. All reactors were shaken manually at least three times per day and before sampling. Fluid/precipitate suspensions were sampled regularly from each reactor.

The suspensions were first centrifuged at 23,000 rpm to separate solids from the liquid phases. Then the liquids were filtered through 0.2 μm polycarbonate filters and diluted with 0.1 M HNO_3 before analyses. Aqueous lanthanum and neodymium concentrations were measured with Inductive Coupled Plasma Mass Spectrometry (ICP-MS) using an Agilent Technologies 7500 ce with an uncertainty of ±5%. Total aqueous phosphorus was analyzed by the ascorbic–molybdate blue method (Kuo 1996) using a 3000Series UV/Visible Cecil CE3041 spectrophotometer at a wavelength of 882 nm, with an uncertainty of ±10%.

Measured solution compositions were used to assess solute speciation and mineral saturation states with the aid of PHREEQC (Parkhurst 1998) together with its llnl database (Johnson et al. 2000). This thermodynamic model adopts a standard state of unit activity for pure phases and H_2O at any temperature and pressure. For aqueous species other than H_2O, the standard state is unit activity of the species in a hypothetical 1 molal solution referenced to infinite dilution at any temperature and pressure. The ion activity product (IAP) of La or Nd–rhabdophane was calculated assuming they precipitate according to:

$$REE^{3+} + PO_4^{3-} + nH_2O = REEPO_4 \cdot nH_2O, \quad (1)$$

where REE^{3+} represents either aqueous lanthanum or neodymium. Consistent with the standard state, the IAP of rhabdophane is given by:

$$IAP = a_{REE^{3+}}\, a_{PO_4^{3-}}, \quad (2)$$

where a refers to the activity of the subscripted aqueous species.

After separation from the supernatant solutions, all solid phases were washed three times with Milli-Q water and subsequently dried at room temperature. X-ray powder diffraction (XRD) analyses were performed using a Philips PW1050 diffractometer and Cu-K_α radiation ($\lambda = 1.5406$ Å). Scans were recorded between 10 and 65° 2θ at a 0.1°/min scan rate and a step size of 0.01°. Patterns were compared to the standard mineral files compiled in the PDF2 database (JCPDS, International Center for Diffraction Data). Crystallite size was calculated using the Scherrer equation (Scherrer 1918). The (111) reflection of a silicon standard (PDF 05-0565) was compared to the $\sim$29° 2θ peak of all samples. Mid-infrared spectra of the solids were acquired from 650 to 4000 cm^{-1} using an A2-Technology MicroLab Portable mid-Infra Red (FTIR) spectrometer, with a diamond internal reflection (DATR) sampling system. Spectra were recorded with a 4 cm^{-1} resolution by co-adding 128 scans. Spectral manipulation including baseline adjustment, smoothing, normalization, and band component analysis was performed using the Thermo Nicolet OMNIC E.S.P. 5.1 software package. Selected solid samples were imaged with a JEOL 1200-MIALL Transmission Electron Microscope (TEM) at 80 keV. Photomicrographs were digitized and crystal dimensions were measured by calculating the best fit of an ellipse to the contours of the crystals using the ImageJ software (Rasband 1997–2009), with 150 and 100 crystals analyzed for the La and Nd–rhabdophane, respectively. The specific surface area of all solid samples was determined by BET (Brunauer et al. 1938), using a 11-point nitrogen adsorption fit and a MicroQuantachrome instrument with samples degassed at room temperature for 20 h before analyses.

Results and discussion

Solid phases evolution

Immediately upon mixing of the initial solutions a white (La system) and light pink (Nd system) precipitate formed. The first sample was taken within 60 s after mixing the two initial aqueous solutions; this sample is referred to as having been sampled at $t = 0.02$ h. XRD patterns of the solids taken from experiments at various temperatures and times are shown in Fig. 1. In the lanthanum–phosphate system (Fig. 1a, b), the precipitates match the pure La–rhabdophane reference pattern (PDF 046-1439). After 168 h and at 100 °C the patterns suggest the formation of minor monazite (anhydrous $LaPO_4$, PDF 035-0731) (Fig. 1b, marked with stars). In the neodymium–phosphate system (Fig. 1c, d) the XRD patterns match

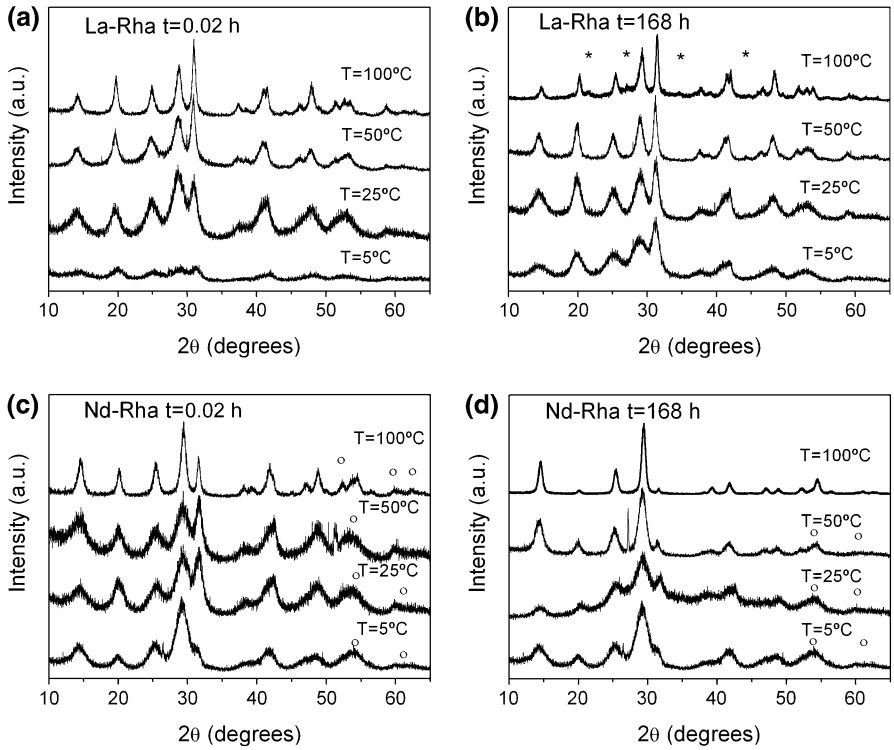

Fig. 1 XRD patterns of solids obtained as a function of temperature. **a** and **b** illustrate the patterns of synthesized La–rhabdophane after 0.02 and 168 h of elapsed time, respectively. The patterns match the reference patterns for synthetic La–rhabdophane, $LaPO_4{\cdot}0.5H_2O$ (PDF 046-1439). At 100 °C and $t = 168$ h some monazite ($LaPO_4$) peaks are evident; peaks corresponding to monazite (PDF 035-0731) are marked with *stars*. **c** and **d** illustrate patterns of synthesized Nd–rhabdophane after 0.02 and 168 h elapsed time, respectively. The patterns match the reference patterns for neodymium phosphate hydrate, $NdPO_4{\cdot}0.5H_2O$, (PDF 034-0535); minor contribution peaks positions from Nd-churchite $NdPO_4{\cdot}2H_2O$ (PDF 039-1385) are indicated by *open circles*

the reference pattern of neodymium phosphate hydrate, $NdPO_4{\cdot}0.5H_2O$ (PDF 034-0535), with minor contribution from Nd–churchite, $NdPO_4\ 2H_2O$ (PDF 039-1385) (Fig. 1c, marked with open circles). Although, a XRD reference pattern is not available for pure Nd–rhabdophane, the structure (hexagonal unit cell and space group P3121) and water content match those of other rhabdophane phases.

In both systems the initially precipitated phases remain stable throughout the experiments, although their crystallinity increased with temperature and time (see Fig. 1). The sharpening of the XRD peaks with temperature and time indicates improved crystallinity in both systems. This was confirmed by the calculated crystallite sizes via the Scherrer equation, using a shape factor $k = 0.94$ (Table 1). Note that crystallite size is the average size of perfect arranged unit cells calculated from the full width at half maximum (FWHM) of XRD peaks (Eq. 3). Scherrer equation crystallite sizes are generally smaller than particles size measured by microscopy, due to a number of factors including non-single crystal, heterogeneous crystal strain, and instrumental effects. At $t = 0.02$ h the crystallite sizes at 5, 25, and 50 °C in both systems were similar and ranged from 2.9 to 4.4 nm. At 100 °C the crystallite size more than doubled to 9.9 nm for the La system and 11.6 nm for the Nd system. The same trends were observed after 168 h. Rajesh et al. (2007) reported a temperature-dependent increase in crystallite size during the transformation from hexagonal to monoclinic monazite. The increase in crystallinity and crystallite size (Table 1) and the appearance of minor monazite at 100 °C in the La system (Fig. 1a) in this study is interpreted to be due to the initiation of the transformation of rhabdophane to monazite at this temperature.

The recovered solids exhibited nano-rod morphologies, as shown by the TEM images in Fig. 2. The particle dimensions (width and length) measured

Table 1 Crystallite sizes determined from XRD patterns, average particle lengths and widths measured by TEM, and specific surface areas (SA_{BET}) of the recovered solids from all experiments

	T (°C)	Crystallite size by XRD[a] (nm)		Average particle length by TEM[b] (nm)		Average particle width by TEM[b] (nm)		SA_{BET}[c] (m^2/g)	
		$t = 0.02$ h	$t = 168$ h	$t = 0.02$ h	$t = 168$ h	$t = 0.02$ h	$t = 168$ h	$t = 0.02$ h	$t = 168$ h
La–Rha	5	3.4	2.6	44 ± 12	54 ± 17	7 ± 2	6 ± 1	–	115
	25	3.4	4	–	–	–	–	97	130
	50	4.4	7.5	–	–	–	–	–	99
	100	9.9	10.5	105 ± 48	116 ± 53	8 ± 3	14 ± 5	–	63
Nd–Rha	5	2.9	3.7	40 ± 14	61 ± 20	5 ± 1	6 ± 2	–	91
	25	3.4	2.3	–	–	–	–	91	114
	50	3.4	6.9	–	–	–	–	–	81
	100	11.6	16.1	94 ± 28	149 ± 70	8 ± 2	14 ± 5	–	54

[a] Crystallite size calculate via Scherrer equation using a shape factor $k = 0.94$

[b] The uncertainties in this table refer to the standard deviation of 150 measurements for the La–PO_4 system and 100 measurements for the Nd–PO_4 system

[c] The precision is ±0.6 m^2/g as determined from the standard deviation of repeated analysis

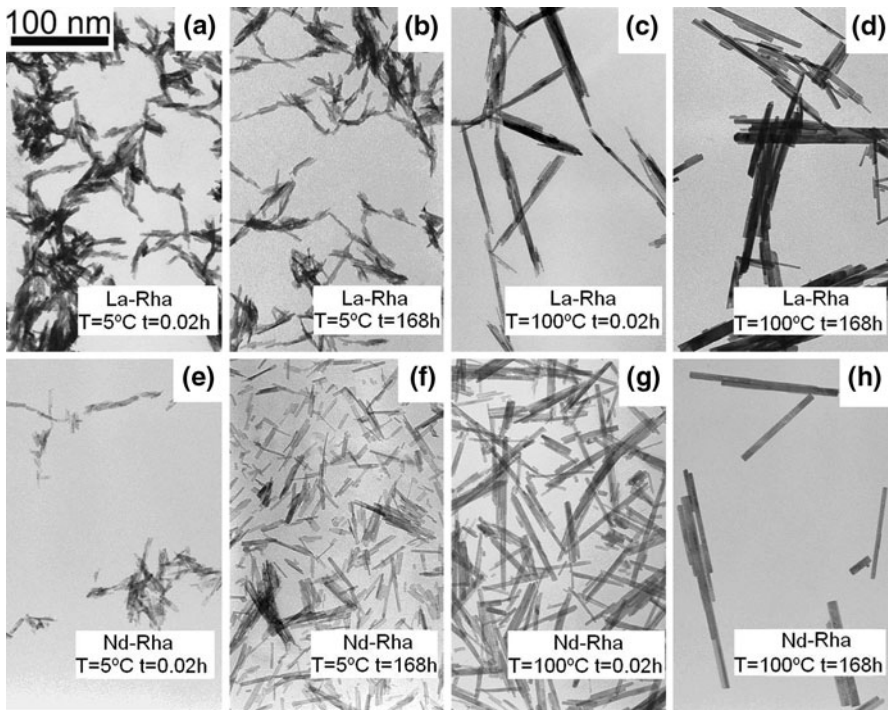

Fig. 2 TEM photomicrographs of La–rhabdophane synthesized at 5 °C (**a**, **b**) and 100 °C (**c**, **d**) at time $t = 0.02$ and 168 h, respectively, Nd–rhabdophane synthesized at 5 °C (**e**, **f**) and 100 °C (**g**, **h**) at time $t = 0.02$ and 168 h, respectively. The *scale bar* showed in **a** is common for all the pictures

from the TEM photomicrographs are shown in Fig. 3 and are provided in Table 1. The data show that the average particle length increased with increasing temperature and time, yet the average widths did not vary significantly. The crystals recovered from the 5 °C La–rhabdophane experiment at $t = 0$ h exhibited a narrow length range from ~18 to 72 nm with an average length of 44 ± 12 nm. After 168 h the nano-rods ranged in length from ~23 to 122 nm with an average length of 54 ± 17 nm. The nano-rods particles synthesized at 100 °C at $t = 0.02$ and 168 h, respectively, exhibited an average length

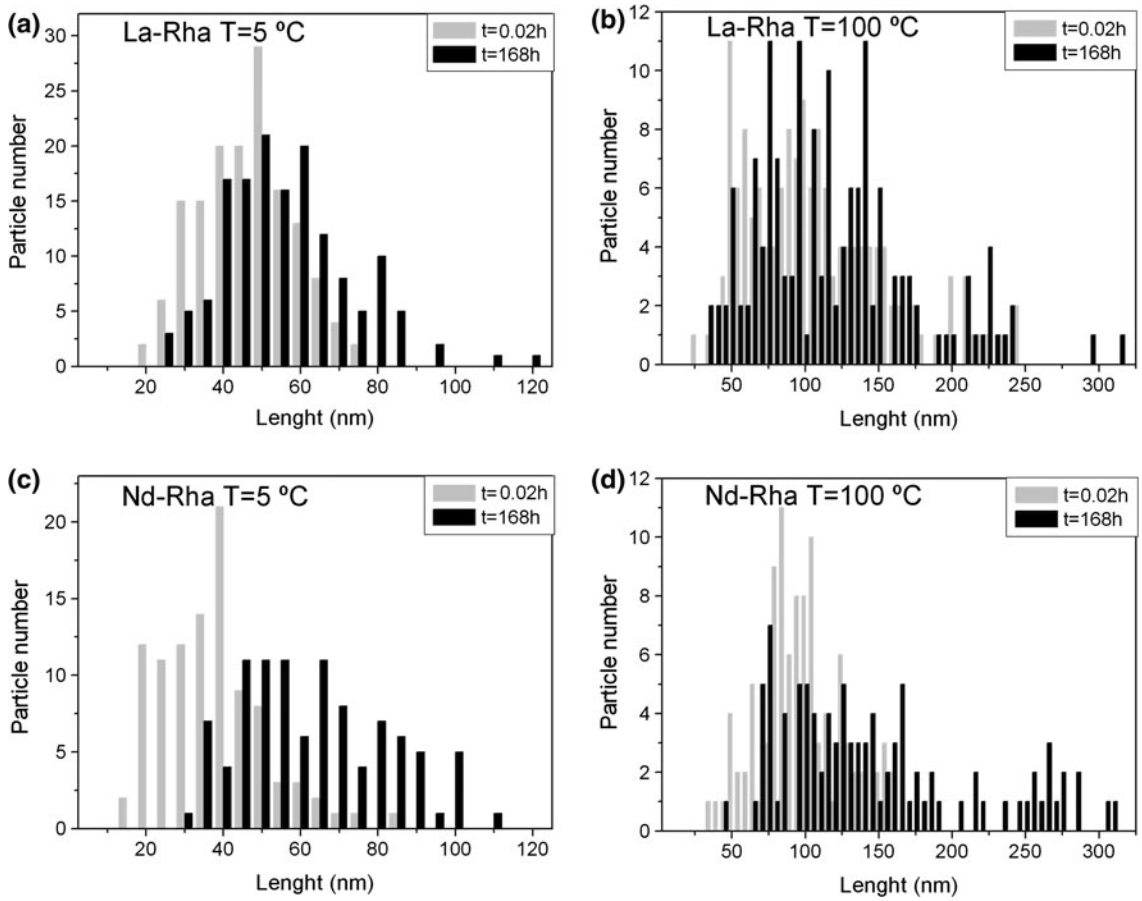

Fig. 3 Particles length obtained at 5 and 100 °C at initial time ($t = 0.02$ h) and at the end of the experiments ($t = 168$ h) from the TEM photomicrographs: **a**, **b** La–rhabdophane and **c**, **d** Nd–rhabdophane. n represents the number of particles measured in each system

of 105 ± 48 nm at $t = 0$ and 116 ± 53 nm at $t = 168$ h, indicating very little change in size with time. For the Nd–rhabdophane system a similar pattern was observed, yet the increase in particle length was more pronounced than in the La system. The Nd–rhabdophane nano-rod particles formed at 5 °C at $t = 0.02$ h had lengths ranging from ~ 17 to 88 nm with an average length of 40 ± 14 nm and after 168 h the lengths reached an average length of 61 ± 20 nm. Interestingly the particles in the Nd system obtained at 100 °C at $t = 0.02$ h had average lengths of 94 ± 30 nm while at $t = 168$ h its length increased to 149 ± 70 nm. The average initial width of the La and Nd–rhabdophane particles was ~ 7 nm and this doubled at 100 °C after 168 h.

The peak positions and bands assignments of solid sample FTIR spectra are shown in Fig. 4 and Table 2. The assignments were based on comparisons with literature data (Assaaoudi et al. 2001; Onoda et al. 2003; Lucas et al. 2004; Morkan et al. 2007; Rajesh et al. 2007; Liu et al. 2008). In both systems the broad band in the 3460–3300 cm^{-1} region (band 1), was assigned to the water O–H stretching vibration. The corresponding H–O–H bending vibration is present at ~ 1645 cm^{-1} (band 2). The peaks between 1200 and 890 cm^{-1} (bands 4–8), correspond to the main P–O interactions. Three v_3 P–O stretching vibrations were observed at ~ 1049, ~ 1065, and ~ 1010 cm^{-1}, and a v_1 P–O stretching vibration was observed at ~ 975 cm^{-1}. In the La–rhabdophane system at

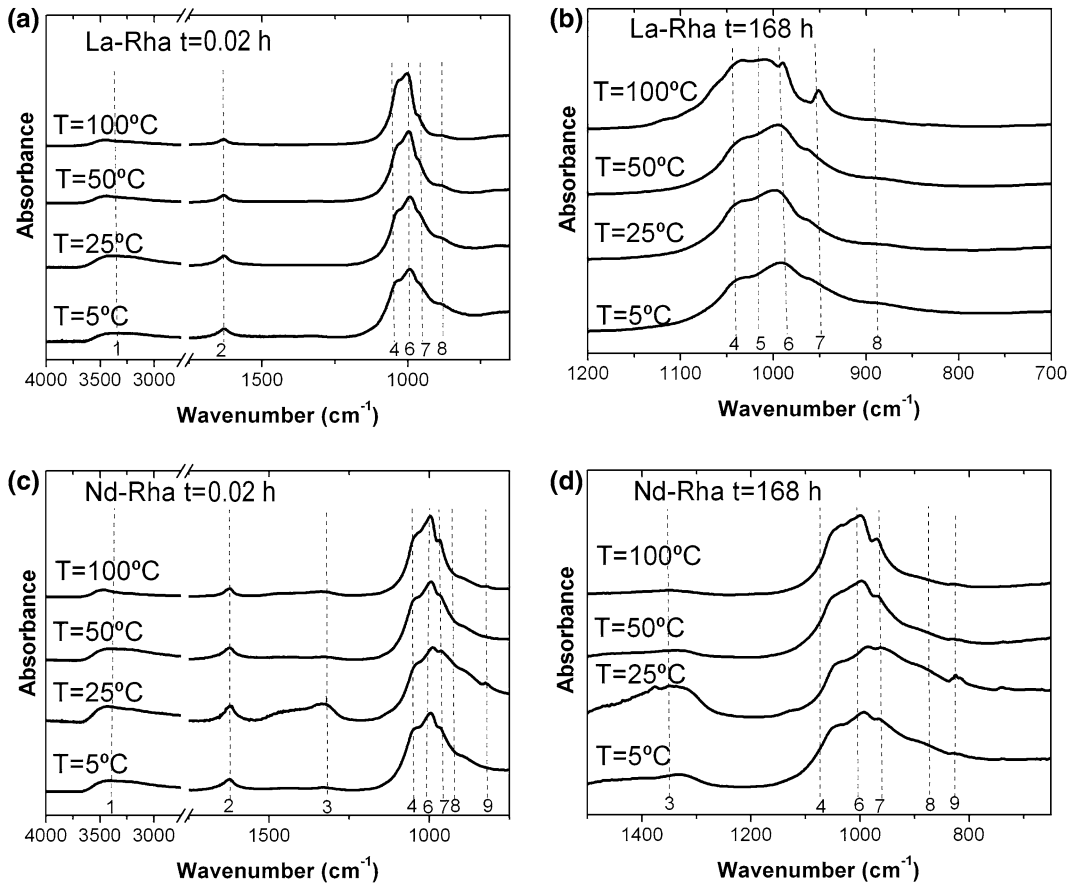

Fig. 4 FTIR spectra as a function of temperature for La–rhabdophane synthesized at time (**a**) $t = 0.02$ and (**b**) 168 h, respectively and Nd–rhabdophane synthesized at time (**c**) $t = 0.02$ and (**d**) 168 h, respectively. The positions of the main bands are indicated by *dashed lines* and *numbers* below the lines correspond to the band assignments listed in Table 2

Table 2 Peak positions of main FTIR bands of the La and Nd–rhabdophane shown in the spectra in Fig. 4

Wavenumber (cm^{-1})				Reference
Band no.	La–Rha	Nd–Rha	Bands assignment[a]	
1	~3480	~3480	O–H *v*	(Lucas et al. 2004)
2	~1645	~1636	H–O–H δ	(Lucas et al. 2004)
3	–	~1350	H–O–N	(Rajesh et al. 2007)
4	~1049	~1067	P–O *v*	(Lucas et al. 2004; Assaaoudi et al. 2001)
5	~1024	–	P–O *v*	(Liu et al. 2008)
6	~1016	~1010	P–O *v*	(Lucas et al. 2004; Onoda et al. 2003)
7	~970	~975	P–O *v*	(Lucas et al. 2004; Assaaoudi et al. 2001)
8	~893	~904	P–O *v*	(Morkan et al. 2007)
9	~840	~841	N–H	(Rajesh et al. 2007)

[a] *v* = stretching; δ = bending

100 °C and after 168 h (Fig. 4b) the peak at ~970 cm^{-1} (band 7) became sharper and another peak at ~1024 cm^{-1} (band 5) representing the contribution from monazite appeared; this observation is consistent with the XRD observations (Fig. 1b). In the Nd–rhabdophane system (Fig. 4c, d) the two bands present at ~1350 and 841 cm^{-1} (bands 3 and 9) likely correspond to nitric acid groups adsorbed onto the rhabdophane particles. These band assignments are based on the study of Rajesh et al. (2007), who observed the appearance of nitrate absorption bands at 1380 and 878 cm^{-1} during the sol–gel synthesis of REE-phosphate. In all cases the phosphate peaks became sharper and better defined with increasing temperature, which is consistent with the XRD results, where a corresponding increase in crystallinity was observed.

The specific surface areas (SA_{BET}) of the recovered solids (Table 1) decreased with increasing temperature confirming the particle size distributions discussed above (Fig. 3). The specific surface areas at 25 °C and $t = 0.02$ h was 97 ± 0.6 and 91 ± 0.6 m^2/g for the La and Nd system, respectively. In the lanthanum system at the end of the experiment ($t = 168$ h), the specific surface area decreased from ~115 ± 0.6 m^2/g at 5 °C to ~63 ± 0.6 m^2/g at 100 °C, while in the neodymium system after 168 h the specific surface area decreased from ~91 ± 0.6 m^2/g at 5 °C to ~54 ± 0.6 m^2/g at 100 °C. These results concur with the observed increase temperature dependent in particles size from the TEM image evaluations and the increase in crystallite size from the XRD determinations.

The REE-phosphate phases precipitated in this study were characterized by nano-rod shapes, high crystallinity, and fairly monodisperse character. These properties are of interest for industrial application and contrasts with other phosphate phases. For example, Mg-phosphates (struvite; $MgNH_4PO_4{\cdot}6H_2O$) precipitates from aqueous fluids at basic conditions as a crystalline phase, but with the formed particles having a twinned "X" morphology with average lengths of 80 μm and widths of 20 μm (Roncal-Herrero and Oelkers 2011). Al and Fe phosphates precipitated from acidic aqueous solutions initially form amorphous phases which transform only slowly (9–21 days) to their crystalline counterparts and in most cases mixed crystalline phases form (Roncal-Herrero et al. 2009). The irregular shape and polycrystallinity of such phosphate phases are not favorable for industrial purposes. Conversely, the La and Nd–rhabdophane synthesized in this study are crystalline with nanometer dimensions and they exhibit narrow size distributions which make then ideally suited for industrial applications (e.g., plasma display panels, solid-state fuel cells, etc.) (Rao and Devine 2000; Norby and Christiansen 1995). Furthermore, as will be shown below, rhabdophane nucleation and growth may be sufficiently fast to also buffer aqueous REE concentrations in natural fluids.

Chemical evolution of the aqueous phase

The evolution of the aqueous fluid compositions as a function of time is listed in Tables 3 and 4. 90% of the initial phosphate and lanthanum or neodymium in the aqueous solutions was removed within the first minute, consistent with REE-phosphate phase precipitation. Also listed in Tables 3 and 4 are the saturation indexes (SI) of these solutions with respect to rhabdophane and REE-hydroxide phases, and the Log (IAP) of the solutions with respect to rhabdophane. The SI given in this table was calculated using:

$$\mathrm{SI} = \mathrm{Log}(\mathrm{IAP}/K), \tag{3}$$

where IAP again refers to the ion activity product and K designates the equilibrium constant of the solid phase as taken from the llnl database (Johnson et al. 2000). This approach uses the Deybe–Hückel equation to calculate activity coefficients as a function of temperature and aqueous solution composition. The SI is positive when the solution is supersaturated with respect to the solid phase, but negative when undersaturated. The calculated SI using equilibrium constants available in the literature suggested that all solutions were supersaturated with respect to rhabdophane at 25 °C, consistent with its precipitation during in the experiments. Equilibrium constant for rhabdophane (Eq. 1) are not available for temperatures others than 25 °C. All solutions were undersaturated with respect to lanthanum and neodymium hydroxides (Tables 3, 4). The aqueous composition evolution in the La-system is consistent with the continuous precipitation of La–rhabdophane and an approach to equilibrium. Although a similar trend is evident for the Nd system, more scatter in the concentrations of the supernatant was observed

Table 3 Chemical evolution of aqueous lanthanum (C_{La}) and phosphorus (C_P) concentrations, SI for selected La phases, and Log (IAP) for the aqueous phase in all La–rhabdophane experiments

T (°C)	Elapsed time (h)	$C_{La} \times 10^4$ mol/L	$C_P \times 10^4$ mol/L	SI[a]			Log (IAP)[b] La–Rha
				La–Rha[c]	$La(OH)_3$	La_2O_3	
5	0	500.00	500.00	–	−17.20	−60.04	−20.83
	0.02	15.80	112.73	–	−18.38	−62.39	−22.25
	0.5	7.26	112.04	–	−18.72	−63.08	−22.57
	3	5.23	112.33	–	−18.87	−63.36	−22.71
	6	4.50	113.74	–	−18.94	−63.50	−22.77
	12	3.78	117.21	–	−19.02	−63.67	−22.84
	24	3.21	118.30	–	−19.09	−63.81	−22.90
	48	3.05	120.82	–	−19.12	−63.87	−22.92
	96	2.14	121.06	–	−19.28	−64.18	−23.07
	168	2.38	121.62	–	−19.23	−64.09	−23.03
25	0	500.00	500.00	4.24	−17.13	−59.88	−20.46
	0.02	7.18	102.88	2.43	−18.60	−62.83	−22.29
	0.5	1.89	106.05	1.87	−19.18	−63.99	−22.85
	3	2.57	104.78	2.00	−19.05	−63.72	−22.72
	6	2.19	105.96	1.93	−19.12	−63.86	−22.78
	12	5.04	107.76	2.29	−18.76	−63.15	−22.42
	24	1.66	109.13	1.82	−19.24	−64.12	−22.90
	48	1.14	110.72	1.66	−19.41	−64.45	−23.05
	96	1.08	110.62	1.64	−19.43	−64.49	−23.08
	168	1.03	113.16	1.62	−19.46	−64.54	−23.09
50	0	500.00	500.00	–	−17.09	−59.81	−20.23
	0.02	3.36	96.97	–	−18.87	−63.36	−22.46
	0.5	1.10	97.59	–	−19.35	−64.33	−22.94
	3	0.57	98.31	–	−19.64	−64.90	−23.22
	6	0.48	100.54	–	−19.72	−65.06	−23.29
	12	0.60	99.42	–	−19.62	−64.86	−23.20
	24	0.32	100.98	–	−19.89	−65.41	−23.46
	48	0.32	100.78	–	−20.02	−65.66	−23.58
	96	0.24	102.47	–	−20.02	−65.66	−23.58
	168	0.25	101.04	–	−20.00	−65.63	−23.57
100	0	500.00	500.00	–	−17.12	−59.86	−20.34
	0.02	0.59	106.37	–	−19.64	−64.91	−23.35
	0.5	0.19	107.72	–	−20.13	−65.89	−23.83
	3	0.11	96.18	–	−20.36	−66.35	−24.11
	6	0.08	95.45	–	−20.50	−66.63	−24.25
	12	0.06	95.38	–	−20.63	−66.88	−24.38
	24	0.05	91.62	–	−20.70	−67.03	−24.47
	48	0.05	95.58	–	−20.70	−67.04	−24.46
	96	0.03	94.22	–	−20.93	−67.48	−24.68
	168	0.03	96.22	–	−20.93	−67.48	−24.68

[a] Calculated using Eq. 3

[b] Calculated using Eq. 2

[c] Calculated using Log $K_{La-Rha} = -24.70$ at 25 °C (Liu and Byrne 1997) according to the reaction $LaPO_4 \cdot 10H_2O = La^{3+} + PO_4^{3-} + 10H_2O$

Table 4 Chemical evolution of aqueous neodymium (C_{Nd}) and phosphorus (C_P) concentrations, SI for selected Nd phases, and Log (IAP) for the aqueous phase in all Nd–rhabdophane experiments

T (°C)	Elapsed time (h)	$C_{Nd} \times 10^4$ mol/L	$C_P \times 10^4$ mol/L	SI[a]			Log (IAP)[b] Nd–Rha
				Nd–Rha[c]	$Nd(OH)_3$	Nd_2O_3	
5	0	500.00	500.00	–	−14.92	−52.27	−20.64
	0.02	98.54	44.45	–	−15.23	−52.88	−21.82
	0.5	98.11	47.61	–	−15.23	−52.89	−21.79
	3	75.92	37.38	–	−17.94	−58.23	−21.41
	6	73.69	35.95	–	−15.33	−53.08	−21.98
	12	n.m.[d]	n.m.[d]	–	n.c.[e]	n.c.[e]	n.c.[e]
	24	66.32	31.25	–	−15.36	−53.15	−22.06
	48	73.55	41.37	–	−15.34	−53.10	−21.92
	96	76.13	47.06	–	−15.33	−53.09	−21.86
	168	63.89	34.40	–	−15.38	−53.19	−22.04
25	0	500.00	500.00	4.18	−14.86	−52.15	−20.32
	0.02	99.40	8.59	2.27	−15.17	−52.76	−22.24
	0.5	95.23	43.29	2.94	−15.22	−52.86	−21.58
	3	62.67	27.42	3.26	−17.62	−57.60	−21.05
	6	55.43	24.75	2.55	−15.40	−53.23	−21.97
	12	52.51	22.82	2.49	−15.42	−53.27	−22.02
	24	57.52	27.47	2.60	−15.39	−53.21	−21.91
	48	211.20	194.48	3.70	−15.04	−52.51	−20.81
	96	144.87	115.55	3.43	−15.13	−52.68	−21.09
	168	246.79	233.25	3.80	−15.01	−52.44	−20.71
50	0	500.00	500.00	–	−14.84	−52.11	−20.13
	0.02	79.64	28.17	–	−15.28	−52.99	−21.67
	0.5	75.51	37.34	–	−15.31	−53.04	−21.57
	3	116.44	82.02	–	−15.18	−52.79	−21.13
	6	198.87	177.85	–	−15.04	−52.51	−20.69
	12	229.57	216.02	–	−15.01	−52.45	−20.59
	24	78.76	46.51	–	−15.30	−53.02	−21.47
	48	236.19	232.30	–	−15.01	−52.44	−20.55
	96	97.05	78.55	–	−15.24	−52.91	−21.19
	168	48.48	26.60	–	−15.47	−53.36	−21.86
100	0	500.00	500.00	–	−14.88	−52.19	−20.27
	0.02	12.28	12.36	–	−16.05	−54.53	−22.90
	0.5	15.79	6.36	–	−15.96	−54.35	−23.10
	3	14.79	9.37	–	−15.99	−54.42	−22.96
	6	12.45	6.67	–	−16.06	−54.55	−23.18
	12	13.92	4.22	–	−16.01	−54.46	−23.33
	24	11.89	3.67	–	−16.08	−54.58	−23.45
	48	12.04	3.90	–	−16.08	−54.58	−23.42
	96	11.24	4.30	–	−16.10	−54.64	−23.41
	168	15.78	3.66	–	−15.96	−54.35	−23.34

[a] Calculated using Eq 3

[b] Calculated using Eq. 2

[c] Calculated using Log $K_{Nd-Rha} = -24.50$ at 25 °C (Johnson et al. 2000) according to the reaction $NdPO_4 \cdot 10H_2O = Nd^{3+} + PO_4^{3-} + 10H_2O$

[d] n.m.: concentrations were not measured

[e] n.c.: saturation state and Log (IAP) were not calculated

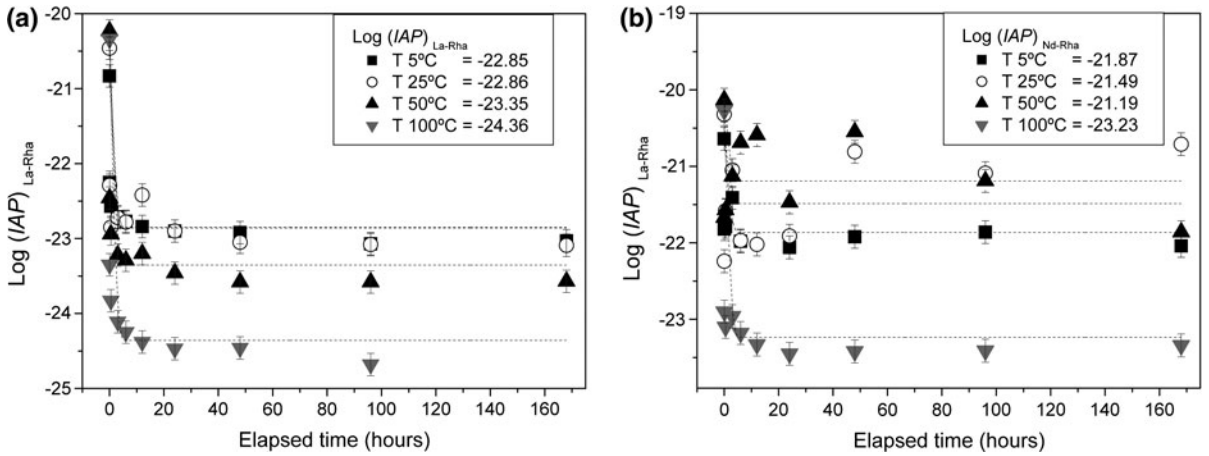

Fig. 5 Change in Log (IAP) as a function of elapsed time for at the indicated temperatures for **a** La–rhabdophane and **b** Nd–rhabdophane. The lines are the best fit to the data points obtained assuming first order exponential decay kinetics

(Table 3, Fig. 5), and this scatter was most obvious in the 25 and 50 °C experiments. The reason for this scatter is unclear, but it could be that small proportion of the nano-rod particles passed through the 0.2 μm filter during the separation of the solids from the reacting solutions. These fine particles could subsequently dissolve when the fluid phase was diluted with 0.1 M HNO_3 before analyses.

Insights into the evolution of the fluid–solid system can be gained by considering the fluid phase ion activity product for potential precipitating phases. The temporal evolution of the Log (IAP) of lanthanum and neodymium rhabdophane in the reactive fluids from the synthesis experiments is presented in Fig. 5. A rapid decrease of Log (IAP) was observed during the first minute of each experiment, consistent with REE–rhabdophane precipitation. Despite the scatter, near-constant Log (IAP) values for both systems were attained at all temperatures after ~40 h. Steady state has been defined as the point where the output La, Nd, or P concentrations were stable within ±15%. These uncertainties in aqueous La or Nd and P concentrations will produce a ±0.15 uncertainty in the calculated Log (IAP). However, the average values of the steady-state Log (IAP) calculated by fitting the experimental data to a first order exponential decay curve revealed that despite marked differences in the goodness of fit (r^2 ~ 0.95 and ~0.45 for La- and Nd-phosphate, respectively), the general trend towards steady state and equilibrium are evident. The average steady-state Log (IAP) for La–rhabdophane decreased from −22.85 at 5 °C to −24.36 at 100 °C, while the average steady-state Log (IAP) for Nd–rhabdophane varied between −21.87 at 5 °C and −23.23 at 100 °C. Although equilibrium between the solid and fluid phases was not confirmed in this study, it seems likely that these steady-state IAP values are close to the equilibrium values for the overall rhabdophane crystallization reaction (e.g., Eq. 1). In general, mineral solubility products are temperature dependent. The IAP of the rhabdophane in the current crystallization study is inversely related to temperature (Tables 3, 4 and Fig. 5). This retrograde behavior has been observed in some other REE-phosphates minerals, including monazite up to at least 300 °C (Cetiner et al. 2005; Poitrasson et al. 2004).

Implications for natural fluids

The results from this study suggest that rhabdophane precipitation from supersaturated solutions is rapid. In nature, rhabdophane is commonly found as alteration products of apatite or basalts (Fodor et al. 1992; Cotton et al. 1995; Berger et al. 2008), while in industrial processes rhabdophane is often precipitated directly from solution like in this study. To assess the role of rhabdophane precipitation in natural environments, a comparison between the compositions of natural water (Gaillardet et al. 2003; Smedley 1991; Johannesson and Lyons 1995; Johannesson et al. 1995, 1996c, b, a; Nordstrom et al. 1992; Stille et al. 2009) and the average steady-state Log (IAP) of La and Nd–rhabdophane determined in this study is

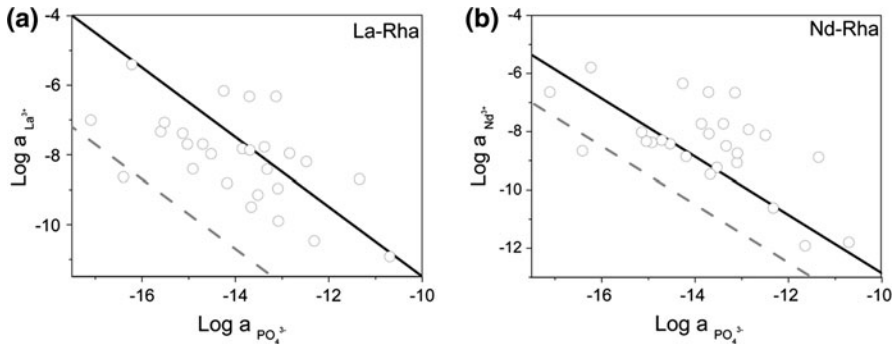

Fig. 6 Logarithms of aqueous La^{3+} or Nd^{3+} activities plotted as a function of corresponding aqueous PO_4^{3-} activities. Circles correspond aqueous activities calculated from the compositions of natural fluids taken from the literature (Gaillardet et al. 2003; Smedley 1991; Johannesson and Lyons 1995; Johannesson et al. 1995; Johannesson et al. 1996c, b, a; Nordstrom et al. 1992; Stille et al. 2009). The *solid line* represents activities for the steady-state IAP of La and Nd–rhabdophane calculated from experiments at 25 °C and the *dotted line* represents activities in equilibrium with rhabdophane according to the llnl database (Johnson et al. 2000)

plotted in Fig. 6a, b, respectively. The La and Nd activities of various natural waters (circles in Fig. 6) lie remarkably close to the solid lines representing the average steady-state Log (IAP) for REE-phosphate calculated from the 25 °C experiments in this study. In contrast, the solutions appear to be supersaturated compared to rhabdophane solubility calculated using the llnl database (Johnson et al. 2000). Small differences between our average steady-state Log (IAP) and the water compositions plotted in Fig. 6 could stem from several factors including: (1) the effect of natural rhabdophane solid-solutions on mineral-fluid equilibrium reaction and (2) uncertainties in the thermodynamic database used to calculate the speciation of the REE and phosphates in the aqueous phase. Nevertheless, our results suggest that La– and Nd–rhabdophane precipitation controls the upper limit on the REEs concentrations of natural solutions.

Conclusions

This study demonstrated experimentally that rhabdophane precipitates directly and equilibrates rapidly with supersaturated solutions at all temperatures from 5 to 100 °C. These results are significant for the understanding of rhabdophane precipitation processes; derived IAP values can serve as an upper limit for REE concentrations in natural systems. This conclusion is confirmed by the close correspondence between the steady-state La and Nd–rhabdophane activity products generated in this study and the compositions of natural fluid. The control of natural REE concentrations by the precipitation of phosphate-bearing minerals provides a rigorous first step in the quantification of "REE compositional spectra" of natural waters. In addition, the data from this study provide the quantitative basis for the large scale production of monodispersed nano-rod rhabdophane materials that have wide applications in industrial processes.

Acknowledgments We would like to thank Sam Shaw, Giuseppe Saldi, Therese K. Flaathen, Tristan Rousseau, and Stacey Callahan for helpful discussions during the course of this study. Lesley Neve, Linda Forbes, Martin Fuller, David Ashley (University of Leeds), and Alain Castillo (CNRS-Université Toulouse) provided technical assistance. Support from CNRS and the European Community through the MIREST and MIN-GRO Network (MEST-CT-2005-021120 and MRTN-CT-2006-035488) is gratefully acknowledged.

References

Andersson PS, Porcelli D, Frank M, Björk G, Dahlqvist R, Gustafsson Ö (2008) Neodymium isotopes in seawater from the Barents Sea and Fram Strait Arctic-Atlantic gateways. Geochim Cosmochim Acta 72:2854–2867

Assaaoudi H, Ennaciri A, Rulmont A (2001) Vibrational spectra of hydrated rare earth orthophosphates. Vibrat Spectrosc 25:81–90

Berger A, Gnos E, Janots E, Fernandez A, Giese J (2008) Formation and composition of rhabdophane, bastnasite and hydrated thorium minerals turing alteration: implications for geochronology and low-temperature processes. Chem Geol 254:238–248

Borrego J, López-González N, Carro B, Lozano-Soria OB (2005) Geochemistry of rare-earth elements in Holocene sediments of an acidic estuary: environmental markers (Tinto river estuary, South-Western Spain). J Geochem Explor 86:119–129

Braun JJ, Viers J, Dupré B, Polvé M, Ndam J, Muller JP (1998) Solid/liquid REE fractionation in the lateritic system of Goyoum, East Cameroon: the implication for the present dynamics of the soil covers of the humid tropical regions. Geochim Cosmochim Acta 62:273–299

Bregiroux D, Lucas S, Champion E, Audubert F, Bernache-Assollant D (2006) Sintering and microstructure of rare earth phosphate ceramics $REPO_4$ with RE = La, Ce or Y. J Eur Ceram Soc 26:279–287

Brunauer S, Emmett P, Teller E (1938) Adsorption of gases in multimolecular layers. J Am Chem Soc 60:309–319

Byrne RH, Kim KH (1993) Rare earth precipitation and coprecipitation behavior: the limiting role of PO_4^{3-} on dissolved rare earth concentrations in seawater. Geochim Cosmochim Acta 57:519–526

Campayo L, Audubert F, Lartigue JE, Botuha S, Bernache-Assollant D (2007) Study of a phosphate-based material with rhabdophane structure for caesium immobilization: synthesis, sintering and leaching behaviour. J Nucl Mat 374:101–108

Cetiner ZS, Wood SA, Gammons CH (2005) The aqueous geochemistry of the rare earth elements. Part XIV. The solubility of rare earth element phosphates from 23 to 150°C. Chem Geol 217:147–169

Chaïrat C, Schott J, Oelkers EH, Lartigue J-E, Harouiya N (2007) Kinetics and mechanism of natural fluorapatite dissolution at 25°C and pH from 3 to 12. Geochim Cosmochim Acta 71:5901–5912

Cotten J, Le Dez A, Bau M, Caroff M, Maury RC, Dulski P, Fourcade S, Bohn M, Brousse R (1995) Origin of anomalous REE and Y enrichments in subaerially exposed basalts-evidence from French-polynesia. Chem Geol 119: 115–138

De Baar HJW, Bacon MP, Brewer PG (1983) Rare-earth distributions with a positive Ce anomaly in the Western North Atlantic Ocean. Nature 301:324–327

Diaz-Guillén JA, Fuentes AF, Gallini S, Colomer MT (2007) A rapid method to obtain nanometric particles of rhabdophane $LaPO_4{\cdot}nH_2O$ by mechanical milling. J Alloys Compd 427:87–93

Fee JA, Gaudette HE, Lyons WB, Long DT (1992) Rare-earth element distribution in Lake Tyrrell groundwaters, Victoria, Australia. Chem Geol 96:67–93

Firsching HF, Brune SN (1991) Solubility products of the trivalent rare earth phosphates. J Chem Eng Data 36:93–95

Fodor RV, Frey FA, Bauer GR, Clague DA (1992) Ages, rare-earth elements enrichment, and petrogenesis of tholeiitic and alkalic basalts from Kahoolawe island, Hawaii. Contrib Miner Petrol 110:442–462

Gaillardet J, Viers J, Dupré B (2003) Trace elements in river waters. In: Holland HD, Turekian KK (eds) Treatise on geochemistry. Pergamon, Oxford, pp 225–272

Gao R, Qian D, Li W (2010) Sol-gel synthesis and photoluminescence of $LaPO_4{:}Eu_3^+$ nanorods. Trans Nonferr Met Soc China 20:432–436

Hannigan RE, Sholkovitz ER (2001) The development of middle REE enrichments in freshwaters: weathering of phosphate minerals. Chem Geol 175:495–508

Hongbing J, Shijie W, Ziyuan O, Shen Z, Chenxing S, Xiuming L, Dequan Z (2004) Geochemistry of red residua underlying dolomites in karst terrains of Yunnan-Guizhou Plateau: II. The mobility of rare earth elements during weathering. Chem Geol 203:29–59

Jeandel C, Bishop JK, Zindler A (1995) Exchange of neodymium and its isotopes between seawater and small and large particles in the Sargasso Sea. Geochim Cosmochim Acta 59:535–547

Johannesson KH, Lyons WB (1995) Rare-earth element geochemistry of Colour Lake, an acidic freshwater lake on Axel Heiberg Island, Northwest Territories, Canada. Chem Geol 119:209–223

Johannesson KH, Stetzenbach KJ, Hodge VF (1995) Speciation of the rare earth element neodymium in groundwater of the Nevada Test Site and Yucca Mountain and implications for actinide solubility. Appl Geochem 10:565–572

Johannesson KH, Lyons WB, Yelken MA, Gaudette HE, Stetzenbach KJ (1996a) Geochemistry of the rare earth element in hypersaline and dilute natural terrestrial waters: complexation behaviour and middle rare-earth elements enrichments. Chem Geol 133:125–144

Johannesson KH, Stetzenbach KJ, Hodge VF, Lyons WB (1996b) Rare earth element complexation behaviour in circumneutral pH groundwaters: assessing the role of carbonate and phosphate ions. Earth Planet Sci Lett 139:305–319

Johannesson KH, Stetzenbach KJ, Hodge VF, Lyons WB (1996c) Replay to comment on the paper "rare earth element complexation behaviour in circumneutral pH groundwaters: assessing the role of carbonate and phosphate ions". Earth Planet Sci Lett 145:139–141

Johannesson KH, Zhou X, Guo C, Stetzenbach KJ, Hodge VF (2000) Origin of rare earth element signatures in groundwaters of circumneutral pH from southern Nevada and eastern California, USA. Chem Geol 164:239–257

Johnson J, Anderson G, Parkhurst D (2000) Database from thermo.com.V8.R6.230 prepared by at Lawrence Livermore National Laboratory, (Revision: 1.11)

Jonasson RG, Bancroft GM, Nesbitt HW (1985) Solubilities of some hydrous REE phosphate with implications for diagenesis and sea water concentrations. Geochim Cosmochim Acta 49:2133–2139

Kijkowska R, Cholewka E, Duszak B (2003) X-ray diffraction and Ir-absorption characteristics of lanthanide orthophosphates obtained by crystallisation from phosphoric acid solution. J Mater Sci 38:223–228

Köhler SJ, Harouiya N, Chaïrat C, Oelkers EH (2005) Experimental studies of REE fractionation during water-mineral interaction: REE release rates during apatite dissolution from pH 2.8 to 9.2. Chem Geol 222:168–182

Kuo S (1996) Phosphorus. In: Sparks DL (ed) Methods of soil analysis, Part 3. Soils Sci Soc Am, Madison

Liu X, Byrne RH (1997) Rare earth and yttrium phosphate solubilities in aqueous solution. Geochim Cosmoch Acta 61:1625–1633

Liu Q, Su Y, Yu H, Han W (2008) YPO4 nanocrystals: preparation and size-induced latticed symmetry enhancement. J Rare Earth 26:495–500

Lucas S, Champion E, Bregiroux D, Bernache-Assollant D, Audubert F (2004) Rare earth phosphate powders RePO4·*n*H2O (Re = La, Ce or Y)–Part I. Synthesis and characterization. J Solid State Chem 177:1302–1311

Min W, Daimon K, Ota T, Matsubara T, Hikichi Y (2000) Synthesis and thermal reactions of rhabdophane-(Yb or Lu). Mater Res Bull 35:2199–2205

Mitchell RS (1965) Rhabdophane from the Chamion Pegmatite, Amelia County, Virginia. Am Mineral 50:231–235

Mooney CL (1950) X-ray diffraction study of cerous phosphate and related crystals. I. Hexagonal modification. Acta Crystallogr 3:337–340

Morkan AU, Morkan I, Demirözü-Şenol S, Güler A (2007) Intermediate products in solid-state reactions of gadolinium oxide and ammonium dihydrogen phosphate. Cryst Res Technol 42:1007–1013

Mourier B, Poulenard J, Chauvel C, Faivre P, Carcaillet C (2008) Distinguishing subalpine soil types using extractible Al and Fe fractions and REE geochemistry. Geoderma 145:107–120

Nedelec JM, Avignant D, Mahiou R (2002) Soft chemistry routes to YPO_4-based phosphors: dependence of textural and optical properties on synthesis pathways. Chem Mater 14:651–655

Norby T, Christiansen N (1995) Proton conduction in Ca- and Sr-substituted $LaPO_4$. Solid State Ionics 77:240–243

Nordstrom DK, McNutt RH, Puigdomènech I, Smellie JAT, Wolf M (1992) Ground water chemistry and geochemical modeling of water–rock interactions at the Osamu Utsumi mine and the Morro do Ferro analogue study sites, Poços de Caldas, Minas Gerais, Brazil. J Geochem Explor 45:249–287

Oelkers EH, Montel J-M (2008) Phosphates and nuclear waste storage. Elements 4:113–116

Oelkers EH, Valsami-Jones E, Roncal-Herrero T (2008) Phosphate mineral reactivity: from global cycles to sustainable development. Mineral Mag 72:337–340

Onoda H, Nariai H, Maki H, Motooka I (2003) Mechanochemical effects on synthesis of rhabdophane-type neodymium and cerium phosphates. Mater Chem Phys 78:400–404

Parkhurst D (1998) PHREEQC (Version 2)-A Computer Program for Speciation, Batch-Reaction, One Dimensional Transport, and Inverse Geochemical Calculations. USGS Water Res Invest.Report 99. Available from: http://wwwbrr.cr.usgs.gov/projects/GWC_coupled/phreeqc/

Poitrasson F, Oelkers EH, Schott J, Montel J-M (2004) Experimental determination of synthetic $NdPO_4$ monazite end-member solubility in water from 21°C to 300°C: implications for rare earth elements mobility in crustal fluids. Geochim Cosmochim Acta 68:2207–2221

Rajesh K, Shajesh P, Seidel O, Mukundan P, Warrier KGK (2007) A facile sol–gel strategy for the synthesis of rod-shaped, nanocrystalline, high-surface-area lanthanum phosphate powder and nanocoatings. Adv Funct Mater 17:1682–1690

Rao CNR, Devine DJ (2000) RE-activated lanthanide phosphate phosphors for PDP applications. J Lumin 87–89:1260–1263

Rasband WS (1997–2009) ImageJ. National Institutes of Health, Bethesda, Maryland, USA. http://rsb.info.nih.gov/ij/index.html

Roncal-Herrero T, Oelkers EH (2011) Experimental study of struvite dissolution and precipitation rates as a function of pH. Appl Geochem. doi:10.1016/j.apgeochem.2011.03.002

Roncal-Herrero T, Rodriguez-Blanco JD, Benning LG, Oelkers EH (2009) The precipitation of iron and aluminium phosphates directly from aqueous solution as a function of temperature from 50 to 200°C. Crys Growth Des 9:5197–5205

Scherrer P (1918) Estimation of the size and internal structure of colloidal particles by means of röntgen. Nachr Ges Wiss Götingen, Math-Pys. Kl. 2:96–100

Smedley PL (1991) The geochemistry of rare Herat elelments in groundwater from the Carnmellis area, southwest England. Geochim Cosmochim Acta 55:2767–2779

Stille P, Pierret MC, Steinmann M, Chabaux F, Boutin R, Aubert D, Pourcelot L, Morvan G (2009) Impact of atmospheric deposition, biogeochemical cycling and water–mineral interaction on REE fractionation in acidic surface soils and soil water (the Strengbach case). Chem Geol 264:173–186

Tanaka K, Kawabe I (2006) REE abundances in ancient seawater inferred from marine limestone and experimental REE partition coefficients between calcite and aqueous solution. Chem J 40:425–435

Taunton AE, Welch SA, Banfield JF (2000) Microbial controls on phosphate and lanthanide distributions during granite weathering and soil formation. Chem Geol 169:371–382

Tosiani T, Loubet M, Viers J, Valladon M, Tapia J, Marrero S, Yanes C, Ramirez A, Dupre B (2004) Major and trace elements in river-borne materials from the Cuyuni basin (southern Venezuela): evidence for organo-colloidal control on the dissolved load and element redistribution between the suspended and dissolved load. Chem Geol 211:305–334

Welch SA, Christy AG, Isaacson L, Kirste D (2009) Mineralogical control of rare earth elements in acid sulfate soils. Geochim Cosmochim Acta 73:44–64

Wood SA (1990) The aqueous geochemistry of rare-earth elements and Y. 1 review of available low-temperature data for inorganic complexes and the inorganic REE speciation of natural waters. Chem Geol 82:159–186

Zhang Y, Guan H (2005) The growth of lanthanum phosphate (rhabdophane) nanofibers via the hydrothermal method. Mater Res Bull 40:1536–1543